The three-dimensional distribution of clouds around Southern Hemisphere extratropical cyclones

Pallavi D. Govekar,[1] Christian Jakob,[1] Michael J. Reeder,[1] and John Haynes[2]

Received 5 August 2011; revised 9 October 2011; accepted 11 October 2011; published 8 November 2011.

[1] The organization and, for the first time, the three-dimensional structure of clouds associated with the Southern Hemisphere cyclones are studied using active observations from the CloudSat and CALIPSO satellites. First, a composite cyclone is constructed from more than 800 individual cases in the years 2007 and 2008 using the cyclone centre as the composite reference point. It is shown that the three-dimensional cloud distribution around the composite cyclone agrees well with conceptual models of extratropical cyclones. Composite mean fields of sea level pressure, vertical motion, potential temperature and relative humidity are superposed on the three-dimensional cloud structure to better define the relationship between the clouds and dynamical properties of extratropical cyclones. The methodology used here reveals the relationship between dynamical and cloud processes in three dimensions around cyclones and provides the foundation for in-depth evaluations of the ability of climate models to simulate the cloud and dynamical structures of Southern Hemisphere extratropical cyclones.
Citation: Govekar, P. D., C. Jakob, M. J. Reeder, and J. Haynes (2011), The three-dimensional distribution of clouds around Southern Hemisphere extratropical cyclones, *Geophys. Res. Lett.*, *38*, L21805, doi:10.1029/2011GL049091.

1. Introduction

[2] The reports of the Intergovernmental Panel for Climate Change (IPCC) have all highlighted clouds and cloud feedbacks as major uncertainties in our understanding of the climate system and a limitation in our ability to project changes to this system. For example, the WG1 report of AR4 [*Intergovernmental Panel on Climate Change*, 2007] states that "despite some advances in the understanding of the physical processes that control the cloud response to climate change and in the evaluation of some components of cloud feedbacks in current models, it is not yet possible to assess which of the model estimates of cloud feedback is most reliable." Moreover, clouds are strongly associated with the major circulation systems of the planet and for this reason satellite imagery is extensively used to identify circulation systems such as extratropical and tropical cyclones as well as the convective systems that comprise the Intertropical Convergence Zone.

[3] Since the advent of satellites the global distribution of clouds has been studied extensively [e.g., *Rossow and Schiffer*, 1999, and references therein], although those in the Southern Hemisphere extratropics have received less attention than their Northern Hemisphere counterparts [e.g., *Troup and Streten*, 1991; *Jones and Henderson-Sellers*, 1992; *Gordon and Norris*, 2010; *Haynes et al.*, 2011]. As the background albedo is low over the Southern Ocean, the energy budget is very sensitive to the presence of clouds [*Cess et al.*, 1990]. Recently, clouds over the Southern Ocean have been the subject of increased interest due to mounting evidence of their poor representation in climate models [*Trenberth and Fasullo*, 2010].

[4] The Southern Ocean storm tracks and their associated extratropical cyclones [*Simmonds and Keay*, 2000] and fronts [*Berry et al.*, 2011] are prominent features of the Southern Hemisphere, and the cloud fields associated with these systems have a major effect on the radiative balance [*Haynes et al.*, 2011].

[5] Clouds around extratropical cyclones are strongly organized by the internal circulations that accompany these baroclinic systems. *Bjerknes and Solberg* [1922] first explained the relative movement of different air masses along inclined frontal surfaces in extratropical cyclones and related the pattern of clouds and precipitation to vertical air motion. Their conceptual model was so successful that it was not substantially altered until *Shapiro and Keyser* [1990] incorporated a frontal fracture early in the life cycle, the frontal T-bone and bent-back warm front at the midpoint of the life cycle, and a warm-core seclusion near the end of the life cycle. With the advent of passive satellite remote sensing, many of the dynamical, cloud and precipitation features of extratropical cyclones have been studied through case studies [*Browning and Roberts*, 1994; *Posselt et al.*, 2008] and through cyclone compositing [*Lau and Crane*, 1995; *Tselioudis and Rossow*, 2006; *Catto et al.*, 2010]. *Lau and Crane* [1995] used data from the International Satellite Cloud Climatology Project [*Rossow and Schiffer*, 1999] in a composite of approximately 200 cyclones to provide a detailed view of the synoptic organization of clouds. An important limitation of studies based on passive remote sensing from satellites is that the retrieved cloud information usually represents the properties at or near cloud top or, in the case of thin cloud layers, represents a mix of properties from different levels in the atmosphere that is difficult to disentangle. The recent launch of active remote sensors on board the CloudSat [*Stephens et al.*, 2008] and CALIPSO [*Winker et al.*, 2007] satellites that form part of the A-Train satellite constellation [*Stephens et al.*, 2002] provides, for the first time, an opportunity to combine observations of the cloud, radiation and precipitation with reanalyses of the circulation and thermodynamic structure to form a fairly complete composite picture of the Southern Ocean extratropical cyclones.

[1] Monash Weather and Climate, School of Mathematical Sciences, Monash University, Clayton, Victoria, Australia.
[2] Cooperative Institute for Research in the Atmosphere, Colorado State University, Fort Collins, Colorado, USA.

0094-8276/11/2011GL049091

[6] The Cloudsat/CALIPSO data set provides a unique opportunity to construct a comprehensive three-dimensional cloud distribution surrounding the synoptic storms from observations [e.g., *Naud et al.*, 2010]. Our goal is to depict with these data the three dimensional structure of clouds around Southern Hemisphere extratropical cyclones using a compositing method very similar to that of *Lau and Crane* [1995]. The present study also builds on the recent studies by *Naud et al.* [2010], who demonstrated the utility of CloudSat/CALIPSO data in studying the aggregate three-dimensional cloud distribution associated with frontal systems, and by *Posselt et al.* [2008] who, with case studies, showed the potential of using CloudSat/CALIPSO to add the third dimension to the study of extratropical systems. Since the sampling of clouds by the CloudSat/CALIPSO instruments is much more sparse than that by passive instruments, a much larger number of cyclones than used in previous work needs to be included in the composites. Here 880 cyclones are used, out of which 78 were observed in December-February (DJF), 218 in March–May (MAM), 447 in June–August (JJA) and 137 in September–November (SON).

2. Constructing the Composite Cyclone Cloud Structure

[7] The first step in the analysis is to identify and track cyclones over the Southern Ocean using the MAP Climatology of Midlatitude Storminess (MCMS) [*Bauer and DelGenio*, 2006]. The MCMS technique identifies cyclones by minima in sea level pressure (SLP) and assigns a simple intensity classification to each cyclone. This is done by finding the distribution of central SLP (by hemisphere and season) and assigning to it one of three intensities. Intensity 1 denotes a weak cyclone in the lower third of the distribution, intensity 2 denotes a moderate cyclone in the middle third, and intensity 3 denotes a strong cyclone in the upper third of the distribution. Only cyclones of intensity 2 are used here so that the composite comprises cyclones of similar strength. As a first step in compositing, cyclones in the latitudinal band 40°S–50°S for the years 2007 and 2008 are identified. Then, cyclone centers of intensity 2 located within the 40°S–50°S latitudinal belt are identified. As the longitudinal extent of the cyclones vary with latitude, a grid based on distance is chosen for the compositing [*Field and Wood*, 2007]. A 2000 km × 2000 km grid box (x and y are the eastward and northward coordinates, respectively), is drawn around each identified cyclone centre and a new coordinate system, with 100 km grid spacing, is defined with the cyclone centre as its central point (x = 0, y = 0). Finally, all the cyclones are overlaid in a new cyclone-relative coordinate system.

[8] Some studies have composited cyclones using a cylindrical polar coordinate system and suggested the need to rotate the cyclones according to their direction of propagation [*Rudeva and Gulev*, 2011; *Catto et al.*, 2010, and references therein]. The main reason for this rotation is to better align frontal systems and their associated wind and cloud fields in the composites. As the main aim here is to study the cloud structures associated with the cyclones, it is important to test whether rotation is required. To do this an objective algorithm to identify fronts using wet bulb temperature (θ_w) at 850 hPa [*Berry et al.*, 2011] is applied to the NCEP-DOE AMIP-II Reanalysis [*Kanamitsu et al.*, 2002]. The number of occurrences of cold and warm fronts in each of the 100 km × 100 km grid boxes of the composite is determined. Isolines of one third of the maximum value of occurrence of warm and cold fronts are plotted in Figure 1 to identify the most common locations of the fronts in the cyclones that comprise the composite. It is evident that the fronts are well organized within the cyclone composite and adhere to the idealized picture of frontal locations in extratropical cyclones [*Bjerknes and Solberg*, 1922; *Shapiro and Keyser*, 1990]. Cold fronts are located to the north of the cyclone centre while warm fronts are located on its eastern side. While there is some spread in the location of the fronts, the overall structures are clearly identifiable, leading us to conclude that rotation of the cyclones is not essential for the present study. It is worth noting that cyclones are composited over all stages of development and the resulting composite cannot be expected to display the well-known development-stage dependent tilt of the systems [*Lim and Simmonds*, 2007].

[9] The next step is to construct a three-dimensional picture of the cloud structure around the composite cyclone. For this purpose the 2B-GEOPROF-LIDAR product is used as it combines the Cloud Profile Radar (CPR) data from the CloudSat satellite with the CALIOP lidar data from the CALIPSO satellite [*Mace et al.*, 2009]. A pixel is defined to be cloudy if either the CloudSat radar indicates the existence of a cloud (i.e., a cloud mask value of 30 or higher) or the CALIOP lidar indicates that the radar bin in question contains 50% or greater cloud cover.

[10] For each of the cyclones in the composite, all of the CloudSat/CALIPSO orbits intersecting the 2000 km × 2000 km cyclone area box are found. Of the 880 cyclones in the original composite, 816 have Cloudsat/CALIPSO orbits intersecting them, and these are used to form the composite of the cloud structure. As with the analysis of fronts the cyclone area box is divided into 100 km × 100 km boxes and GEOPROF pixels are assigned to the appropriate box for each cyclone. The cloudy and total pixels falling into each box are counted to give the cloud fraction in each 240-m height bin around the composite cyclone.

[11] As cloud structures are invariably linked to the internal circulations that accompany of the cyclone, some selected dynamical fields are composited and superposed on the three-dimensional cloud structure. To do so, 6-hourly NCEP-DOE AMIP-II reanalysis data at 2.5° × 2.5° horizontal resolution and 17 pressure levels (hPa) are regridded and composited for the cyclones that also have CloudSat and CALIPSO data. Finally, composites of the radiation and precipitation information around the cyclone centres are constructed. At the top of atmosphere (TOA), cloud radiative effect (CRE) composites, i.e., the difference between clear sky and full sky conditions for both shortwave and longwave radiation [*Ramanathan et al.*, 1989], are constructed for the year 2007 using the ISCCP-FD data set [*Zhang et al.*, 2004]. Daily GPCP data [*Huffman et al.*, 2001] is used to construct the composite precipitation field around the cyclone.

3. Results

[12] Figure 1 shows slices of the composite three-dimensional cyclone in the horizontal and in the vertical.

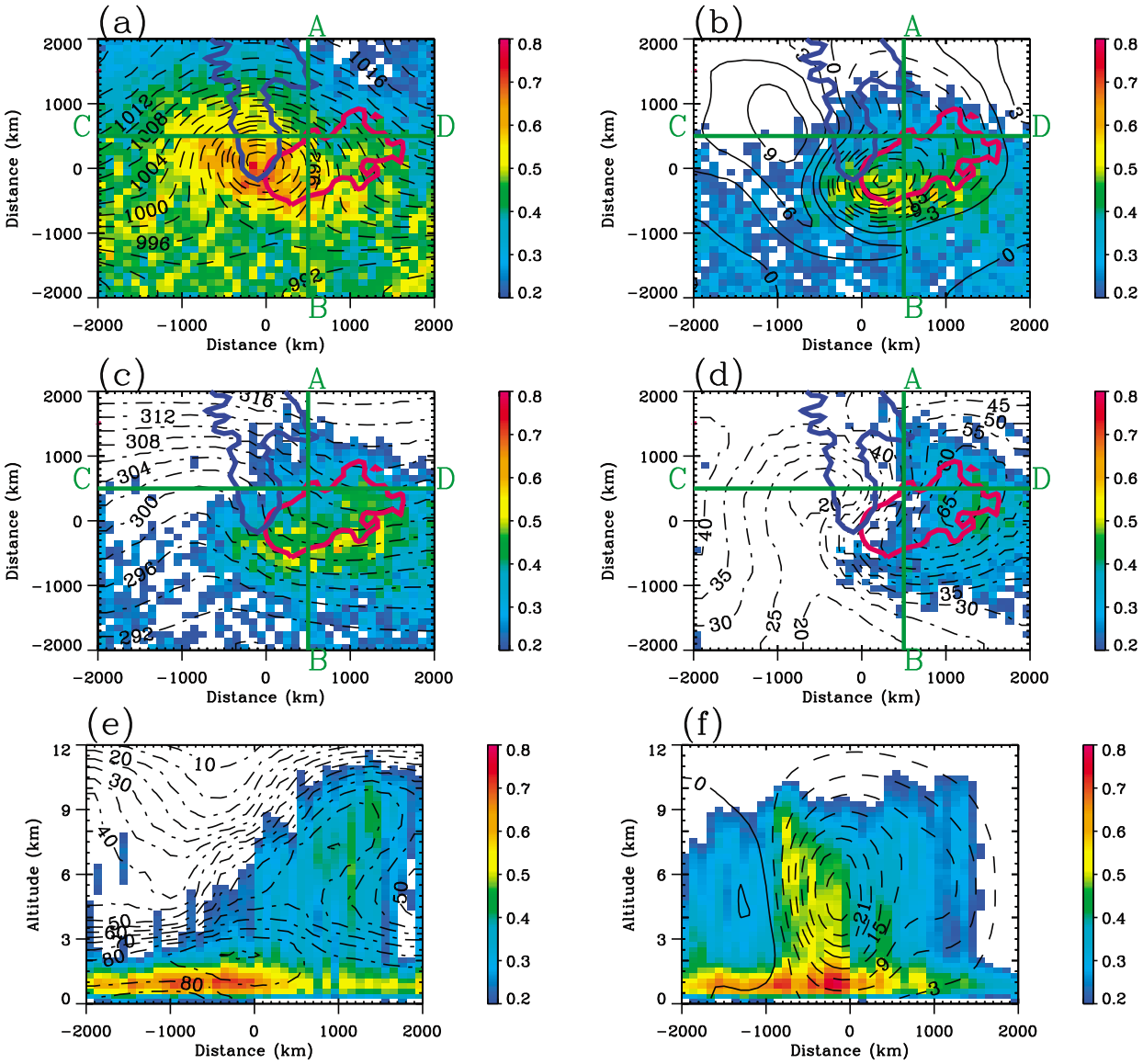

Figure 1. Cloud and dynamical structure of the composite cyclone. Dynamical fields are contoured, cloud fields are shaded and isolines of the occurrence of cold and warm fronts are shown by blue and red lines, respectively. In first four panels, Lines CD and AB indicate the position of the cross-sections shown in Figures 1e and 1f, respectively. (a) Cloud fraction at 1.75 km and mean sea level pressure (hPa). (b) Cloud fraction and ω (10^{-2} hPa/s) at 4.25 km. (c) Cloud fraction and potential temperature (K) at 6.25 km. (d) Cloud fraction and relative humidity (%) at 9.25 km. (e) Cross section of relative humidity and cloud fraction along the line CD. (f) Cross section of ω and cloud fraction along the line AB.

The mean cloud field at a height of 1.75 km and the composite mean sea level pressure (MSLP) are plotted in Figure 1a. The centre of the composite cyclone has a minimum pressure of approximately 980 hPa. The low-level clouds are most numerous in the centre of the cyclone, extending slightly to the southeast and northwest behind the cold frontal region. Low clouds are also common on the southern side of the cyclone centre. This result is consistent with the mean cloud distribution over the Southern Hemisphere [*Haynes et al.*, 2011], which shows ubiquitous low cloudiness of high cloud fraction over much of the Southern Ocean south of 40°S.

[13] Figure 1b shows the vertical motion in pressure co-ordinates, $\omega = dp/dt$ and cloud fraction at height 4.25 km. Negative ω, denoted by dashed lines, indicates regions of ascent while positive ω (solid black line) denotes regions of subsidence. The vertical motion field has a dipole structure with ascent to the east-northeast of the cyclone center, peaking in the warm frontal region and to a lesser extent in the cold frontal regions, and subsidence to the west-southwest of the cyclone centre with a strong peak to the west of the cold frontal region. Not surprisingly the cloud field at this height (typically termed mid-level cloud) mirrors the vertical motion field with a distinct maximum in cloud fraction within or just ahead (to the south) of the warm frontal region. A secondary maximum in mid-level clouds is visible at the southern edge of the composite domain, again consistent with *Haynes et al.* [2011] who showed a maximum in mid-level clouds south of 55°S over the Southern Ocean.

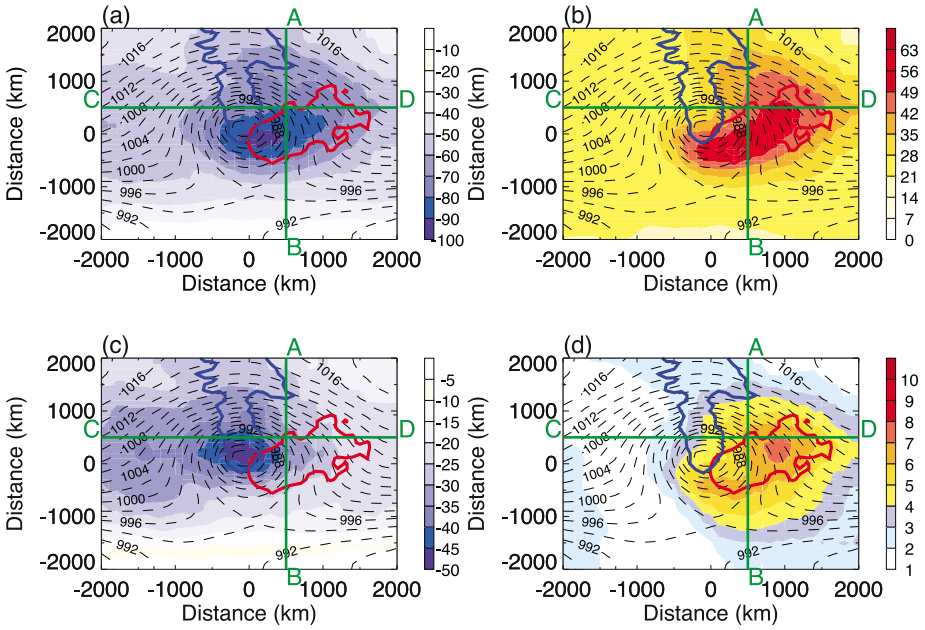

Figure 2. Cyclone composite cloud radiative effect (CRE), MSLP and precipitation. MSLP is contoured, the radiation and precipitation fields are shaded and the isolines of the occurrence of cold and warm fronts are shown by blue and red lines, respectively.(a) Shortwave CRE (W/m^2). (b) Longwave CRE (W/m^2). (c) Net CRE (W/m^2). (d) Precipitation (mm/day). Lines CD and AB indicate the position of cross-sections shown in Figures 1e and 1f, respectively.

[14] Figure 1c shows the mean potential temperature and cloud fraction at 6.25 km. The thermal trough, associated with subsidence, is situated to the west of the cold frontal region and surface low, while the thermal ridge, associated with ascent is situated along the eastern side of the warm frontal region. The maximum cloud fraction is located well to the southeast side of the cyclone centre and poleward of the warm frontal region. Recalling that the fronts are identified at 850 hPa, this is consistent with the tilted cloud structure of warm fronts in conceptual and theoretical models of extratropical cyclones.

[15] Figure 1d shows the cloud fraction and relative humidity (with respect to liquid water) at 9.25 km. There are very high level thin cirrus clouds on the east-northeast side of the cyclone centre just east of the warm frontal region. The relative humidity maximum coincides with the cloud maximum, while regions with low relative humidity coincide with the cloud-free regions to the west of the cyclone centre. Taken together, the cloud fields depicted in Figures 1a–1d are consistent with the classical conveyor belt picture of extratropical cyclones [e.g., *Browning and Roberts*, 1994]. Air parcels ascend and form cloud, while traveling southward ahead of the cold front in what is commonly called the warm conveyor belt. These air parcels ascend the warm front before turning anticyclonically at upper levels. On the cold side the cold front air parcels subside producing the characteristic postfrontal dry slot.

[16] Figure 1e shows an east-west slice of the cloud fraction taken at 500 km in the y-direction (indicated by the line CD in the horizontal slices). Low-level clouds dominate the western half of the cross section, consistent with Figure 1a. These clouds coincide with a region of low mid- and upper tropospheric relative humidity and a strong vertical gradient in relative humidity at around 3 km. The cloud fraction in this region is very high around 1 km and is accompanied by high relative humidity. The low cloud maximum extends into the eastern half of the cross section, indicating the ubiquity of boundary layer clouds over the ocean surface found in many earlier studies [*Rossow and Schiffer*, 1999; *Haynes et al.*, 2011]. The eastern half of the cross section exhibits a tilted cloud and humidity structure closely following the conceptual model of air ascending along the warm conveyor belt in the east-northeastern part of the cyclone. The maximum cloud height is about 11 km with a cloud cover maximum at around 9 km.

[17] Finally, Figure 1f shows a north-south slice of the three-dimensional cloud structure taken at 500 km in the x-direction (indicated by the line AB in the horizontal slices in Figure 1). It is evident from the horizontal cloud maps that the cross-section taken at 500 km in the x-direction crosses the warm frontal region, which extends from roughly −1000 km to 1000 km in the y-direction. Low clouds and subsidence dominate the region south of the main warm frontal zone. Cloud cover maxima at 1 km and 7 km dominate the main warm frontal zone, with maximum cloud height increasing northward along the section reaching levels between 10 and 11 km.

[18] As discussed in Section 1, extratropical cyclones strongly affect the atmospheric energy budget, not only through their dynamical characteristics, but also through the radiative and latent heating effects of their cloud and precipitation structures. Figure 2 shows the distribution of the shortwave, longwave and net cloud radiative effect, as well as the precipitation around the composite cyclone. There is a strong negative cloud effect in the shortwave of more than 50 W/m^2 in most of the area covering −1000 km to 1000 km in the y-direction (cf. Figure 2a). The shortwave negative (cooling) cloud effect is largest just to the southeast of the cyclone centre, where it reaches almost 100 W/m^2. While the largest effects lie in the warm frontal region, there are

wide-spread strong shortwave effects away from that area due to the prevalence of low clouds around the cyclone centre (cf. Figure 1). Longwave cloud radiative effects are generally weaker than the shortwave effects, peaking at about 60 W/m^2 (cf. Figure 2b). As the positive (warming) longwave effects are generally driven by high-level clouds, it is not surprising that the maximum in the longwave effect is located in and slightly ahead of the warm frontal region as this is where the highest cloud tops are found in the composite cyclone (cf. Figure 1). Shortwave and longwave effects largely cancel in the warm frontal region, shifting the maximum of the net cloud radiative effects to the north-west of the cyclone centre (cf. Figure 2c). This result highlights the importance of the low clouds, which are not necessarily related to the frontal regions, in determining the net radiative effects of extratropical cyclones on the climate system [e.g., *Tselioudis and Rossow*, 2006].

[19] Figure 2d shows the distribution of precipitation around the composite cyclone. The area of maximum precipitation lies within and ahead of the warm frontal region, consistent with the location of deep clouds (cf. Figure 1). The significant displacement of the rainfall and cloud maxima to the southeast of the warm frontal region is due to the tilted structure of the cloud systems. Maximum rain rates are in the range of 7–8 mm day^{-1}.

4. Conclusions

[20] The goal of this study was to provide a three-dimensional composite picture of Southern Ocean extratropical cyclone cloud structures using CloudSat and CALIPSO measurements, together with their associated velocity and thermodynamics fields derived from NCEP-DOE AMIP-II reanalyses.

[21] The composite three-dimensional structure of clouds closely resembles the classical conceptual models [*Bjerknes and Solberg*, 1922; *Shapiro and Keyser*, 1990; *Posselt et al.*, 2008; *Naud et al.*, 2010]. Progressively thicker high-top clouds are found in the warm frontal region, which is also the region of maximum rainfall, maximum mid- and upper-level ascent and high relative humidity. Thin cirrus clouds are located at the leading edge of the warm frontal region. A smaller, but still significant, region of thick cloud and precipitation is located along the cold frontal regions to the north of the cyclone. Mid-level cloud extends to the south-east of the cyclone centre. Low-level clouds of various depth are found around the system and form the dominant cloud type in the northwest sector of the cyclone. Thick and high clouds are essentially absent in that region due to strong subsidence behind the frontal systems.

[22] Using case studies, *Posselt et al.* [2008] showed that CloudSat can serve as a potent tool for model assessment. The methodology developed here provides another innovative opportunity for an in-depth evaluation of climate models. After analyzing 24 climate models, *Trenberth and Fasullo* [2010] concluded that almost all the models absorbed too much shortwave radiation over the Southern Ocean, leading to poor representations of the radiation budget and cloud fields in the region. It has also been shown that climate models produce strong positive sea surface temperature (SST) biases where the shortwave radiation is too large [*SenGupta et al.*, 2009], although a causal connection of the two errors has not been conclusively established. The comprehensive picture of an extratropical cyclone painted here provides an interesting new way to evaluate the ability of a climate model to simulate the concurrent cloud, dynamical, radiative and precipitation structures in Southern Hemisphere extratropical cyclones.

[23] **Acknowledgments.** The research in this study is supported by the Australian Research Council's Linkage Project Scheme (LP0883961).
[24] The Editor thanks the two anonymous reviewers for their assistance in evaluating this paper.

References

Bauer, M., and A. D. DelGenio (2006), Composite analysis of winter cyclones in a GCM: Influence on climatological humidity, *J. Clim.*, *19*, 1652–1672.
Berry, G., M. J. Reeder, and C. Jakob (2011), A global climatology of atmospheric fronts, *Geophys. Res. Lett.*, *38*, L04809, doi:10.1029/2010GL046451.
Bjerknes, J., and H. Solberg (1922), Life cycle of cyclones and the polar front theory of atmospheric circulation, *Geophys. Publ.*, *3*, 3–18.
Browning, K. A., and N. M. Roberts (1994), Structure of a frontal cyclone, *Q. J. R. Meteorol. Soc.*, *120*, 1535–1557.
Catto, J. L., L. C. Shaffery, and K. I. Hodges (2010), Can climate models capture the structure of extratropical cyclones?, *J. Clim.*, *23*, 1621–1635.
Cess, R. D., et al. (1990), Intercomparison and interpretation of climate feedback processes in 19 atmospheric general circulation models, *J. Geophys. Res.*, *95*, 16,601–16,615.
Field, P., and R. Wood (2007), Precipitation and cloud structure in midlatitude cyclones, *J. Clim.*, *20*, 233–254.
Gordon, N. D., and J. R. Norris (2010), Cluster analysis of midlatitude oceanic cloud regimes: Mean properties and temperature sensitivity, *Atmos. Chem. Phys.*, *10*, 6435–6459.
Haynes, J. M., C. Jakob, W. B. Rossow, G. Tselioudis, and J. Brown (2011), Major characteristics of Southern Ocean cloud regimes and their effects on the energy budget, *J. Clim*, doi:10.1175/2011JCLI4052.1, in press.
Huffman, G. J., R. Adler, M. Morrissey, D. Bolvin, S. Curtis, R. Joyce, B. McGavock, and J. Susskind (2001), Global precipitation at one-degree daily resolution from multi-satellite observations, *J. Hydrometeorol.*, *2*, 36–50.
Intergovernmental Panel on Climate Change (2007), *Climate Change* 2007*: The Physical Science Basis. Contribution of Working Group I to the Fourth Assessment Report of the Intergovernmental Panel on Climate Change*, edited by S. Solomon et al., Cambridge Univ. Press, Cambridge, U. K.
Jones, P. A., and A. Henderson-Sellers (1992), Historical records of cloudiness and sunshine in Australia, *J. Clim.*, *5*, 260–267.
Kanamitsu, M., W. Ebisuzaki, J. Woollen, S. Yang, J. J. Hnilo, M. Fiorino, and G. L. Potter (2002), NCEP-DOE AMIP-II reanalysis (R-2), *Bull. Am. Meteorol. Soc.*, *83*, 1631–1643.
Lau, N. C., and M. W. Crane (1995), A satellite view of the synoptic-scale organization of cloud properties in midlatitude and tropical circulation systems, *Mon. Weather Rev.*, *123*, 1984–2006.
Lim, E. P., and I. Simmonds (2007), Southern Hemisphere winter extratropical cyclone characteristics and vertical organisation observed with the ERA-40 reanalysis data in 1979–2001, *J. Clim.*, *20*, 2675–2690.
Mace, G. G., Q. Zhang, M. Vaughan, R. Marchand, G. Stephens, C. Trepte, and D. Winker (2009), A description of hydrometeor layer occurrence statistics derived from the first year of merged Cloudsat and CALIPSO data, *J. Geophys. Res.*, *114*, D00A26, doi:10.1029/2007JD009755.
Naud, C. M., A. D. Genio, M. Bauer, and W. Kovari (2010), Cloud vertical distribution across warm and cold fronts in Cloudsat-CALIPSO data and a general circulation model, *J. Clim.*, *23*, 3397–3415.
Posselt, D., G. Stephens, and M. Miller (2008), Cloudsat-Adding a new dimension to a classical view of extratropical cyclones, *Bull. Am. Meteorol. Soc.*, *89*, 599–609.
Ramanathan, V., B. Barkstrom, and E. F. Harrison (1989), Climate and the Earth's radiation budget, *Phys. Today*, *42*(5), 22–33.
Rossow, W. B., and R. A. Schiffer (1999), Advances in understanding clouds from ISCCP, *Bull. Am. Meteorol. Soc.*, *80*, 2261–2287.
Rudeva, I., and S. K. Gulev (2011), Composite analysis of north Atlantic extratropical cyclones in the NCEP reanalysis data, *Mon. Weather Rev.*, *139*, 1419–1446.
SenGupta, A., A. Santoso, A. Taschetto, C. C. Ummenhofer, J. Trevena, and M. H. England (2009), Projected changes to the Southern Hemisphere ocean and sea ice in the IPCC AR4 climate models, *J. Clim.*, *22*, 3047–3078.

Shapiro, M. A., and D. Keyser (1990), Fronts, jet streams, and the tropopause, in *Extratropical Cyclones: The Erik Palmén Memorial Volume*, edited by C. W. Newton and E. O. Halopainen, Am. Meteorol. Soc., Boston, Mass.

Simmonds, I., and K. Keay (2000), Mean Southern Hemisphere extratropical cyclone behaviour in the 40-year NCEP-NCAR reanalysis, *J. Clim.*, *13*, 873–885.

Stephens, G. L., et al. (2002), The Cloudsat mission and the A-TRAIN: A new dimension to space-based observations of clouds and precipitation, *Bull. Am. Meteorol. Soc.*, *83*, 1771–1790.

Stephens, G. L., et al. (2008), CloudSat mission: Performance and early science after the first year of operation, *J. Geophys. Res.*, *113*, D00A18, doi:10.1029/2008JD009982.

Trenberth, K. E., and J. Fasullo (2010), Simulation of present day and 21st century energy budgets of the southern oceans, *J. Clim.*, *23*, 440–454.

Troup, A. J., and N. A. Streten (1991), Satellite-observed Southern Hemisphere cloud vortices in relation to conventional observations, *J. Appl. Meteorol.*, *11*, 909–917.

Tselioudis, G., and W. B. Rossow (2006), Climate feedback implied by observed radiation and precipitation changes with midlatitude storm strength and frequency, *Geophys. Res. Lett.*, *33*, L02704, doi:10.1029/2005GL024513.

Winker, D. M., W. H. Hunt, and M. J. McGill (2007), Initial performance assessment of CALIOP, *Geophys. Res. Lett.*, *34*, L19803, doi:10.1029/2007GL030135.

Zhang, Y., W. B. Rossow, A. A. Lacis, V. Oinas, and M. I. Mishchenko (2004), Calculation of radiative fluxes from the surface to top of atmosphere based on ISCCP and other global data sets: Refinements of the radiative transfer model and the input data, *J. Geophys. Res.*, *109*, D19105, doi:10.1029/2003JD004457.

P. D. Govekar, C. Jakob, and M. J. Reeder, Monash Weather and Climate, School of Mathematical Sciences, Monash University, Clayton, Vic 3800, Australia. (pallavi.govekar@monash.edu)

J. Haynes, Cooperative Institute for Research in the Atmosphere, Colorado State University, Fort Collins, CO 80523-1375, USA.